Opposite Interdecadal Trends of Summer Atmospheric Rivers over East Asia and Western North Pacific in Recent Decades

Wenshuo Huang[1], Lijuan Hua[1], Linhao Zhong[2], YANG YANG[3], and Gong Zhaohui[4]

[1]University of Chinese Academy of Sciences
[2]National Institute of Natural Hazards, Ministry of Emergency Management of China
[3]National Institute of Natural Hazards, Ministry of Emergency Management of China
[4]Institute of Atmospheric Physics, Chinese Academy of Sciences

November 24, 2022

Abstract

The summer atmospheric river (AR) frequency over East Asia and Western North Pacific (EA-WNP) is investigated by multiple AR detection algorithms based on the Atmospheric River Tracking Method Intercomparison Project (ARTMIP) Tier2 reanalysis dataset. The results show that AR frequency during the recent four decades experienced opposite interdecadal shifts, greatly contributing to the interdecadal equatorward trends of EA ARs and poleward trends of WNP ARs with a boundary around 135°E. The opposite variations are mainly influenced by a zonal dipole of integrated water vapor transport with cyclonic and anticyclonic anomalies centered over Taiwan and the ocean to the southeast of Japan, respectively. A major impact of the Pacific Decadal Oscillation and a reinforcement effect due to a zonal wave train from the North Atlantic jointly modulate the pattern. Considering ARs may curve their pathway over EA-WNP, the algorithms based on historical AR shapes should be cautiously used during AR detection.

Geophysical Research Letters

Supporting Information for

Opposite Interdecadal Trends of Summer Atmospheric Rivers over East Asia and Western North Pacific in Recent Decades

Wenshuo Huang[1], Lijuan Hua[1], Linhao Zhong[2], Yang Yang[2] and Zhaohui Gong[3,4]

[1] College of Earth and Planetary Sciences, University of Chinese Academy of Sciences, Beijing 100049, China

[2]National Institute of Natural Hazards, Ministry of Emergency Management of China, Beijing 100085, China

[3]University of Chinese Academy of Sciences, Beijing 100049, China

[4]CAS Key Laboratory of Regional Climate-Environment for Temperate East Asia, Institute of Atmospheric Physics, Chinese Academy of Sciences, Beijing 100029, China

Posted on 24 Nov 2022 — CC-BY-NC 4 — https://doi.org/10.1002/essoar.10512565.1 — This a preprint and has not been peer reviewed. Data may be preliminary.

Contents of this file

Figures S1 to S7 Table S1

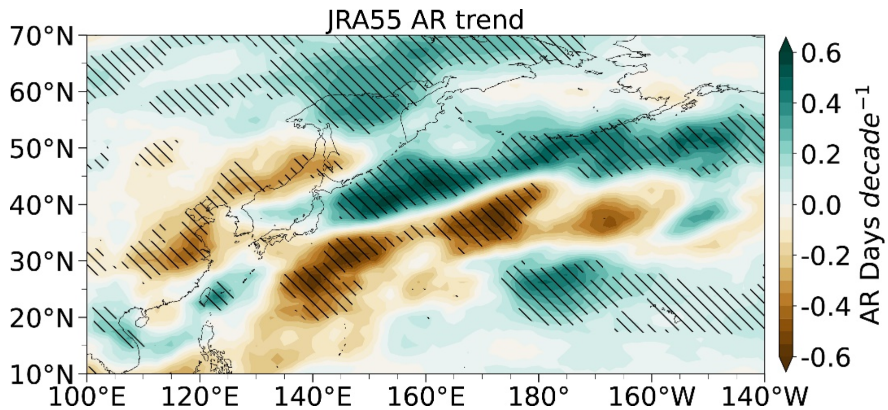

Figure S1. JRA55 JJA-mean AR trends of multiple AR detection algorithm average (Lack of Lora_v2). Black hatches denote the area with a 95% significance level.

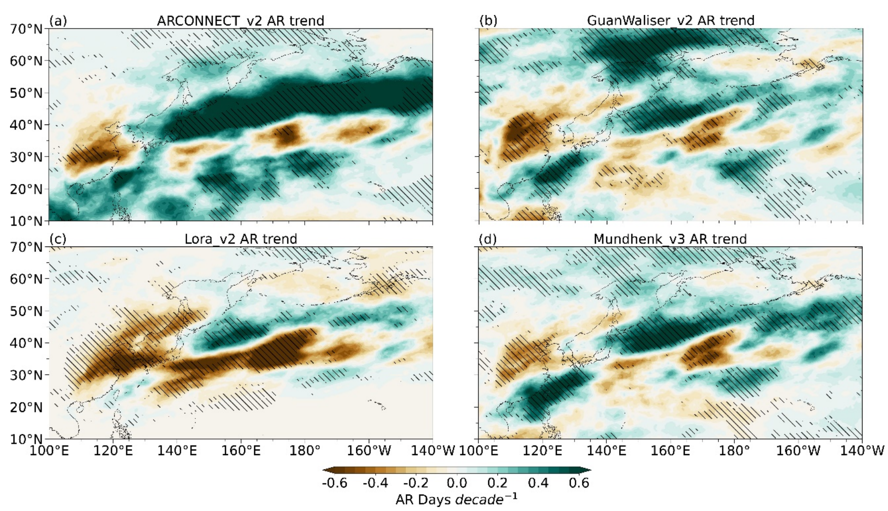

Figure S2. JJA-mean AR trends over EA and WNP of each AR detection algorithm. (a) ARCONNECT_-v2. (b) Guan_Waliser_v2. (3) Lora_v2. (c) Mundhenk_v3. Black hatches in (a)-(d) denote the area with a 95% significance level.

Posted on 24 Nov 2022 — CC-BY-NC 4 — https://doi.org/10.1002/essoar.10512565.1 — This a preprint and has not been peer reviewed. Data may be preliminary.

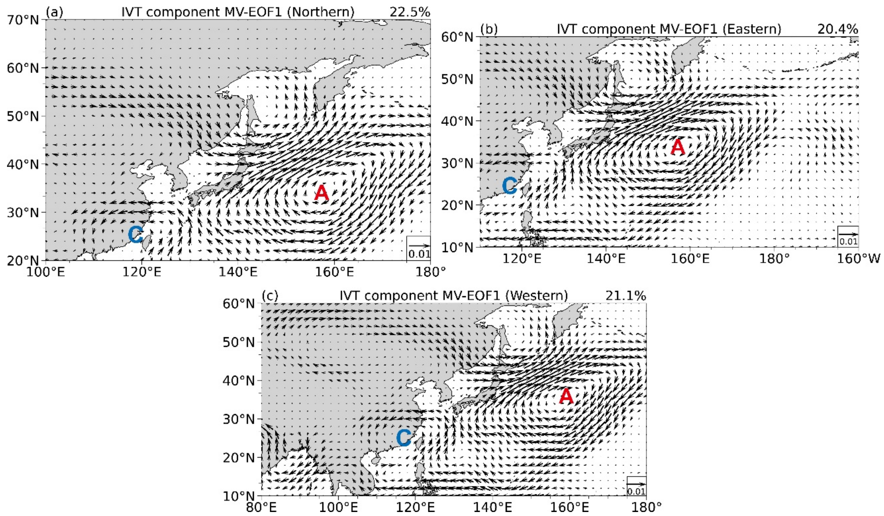

Figure S3. The dominant MV-EOF modes of JJA-mean IVT from different domains. (a) Northern domain (20°–70°N, 100°–180°E). (b) Eastern domain (10°–60°N, 110°E–160°W). (c) Western domain (10°–60°N, 80°–180°E). The fractional variance is noted at the top-right corner.

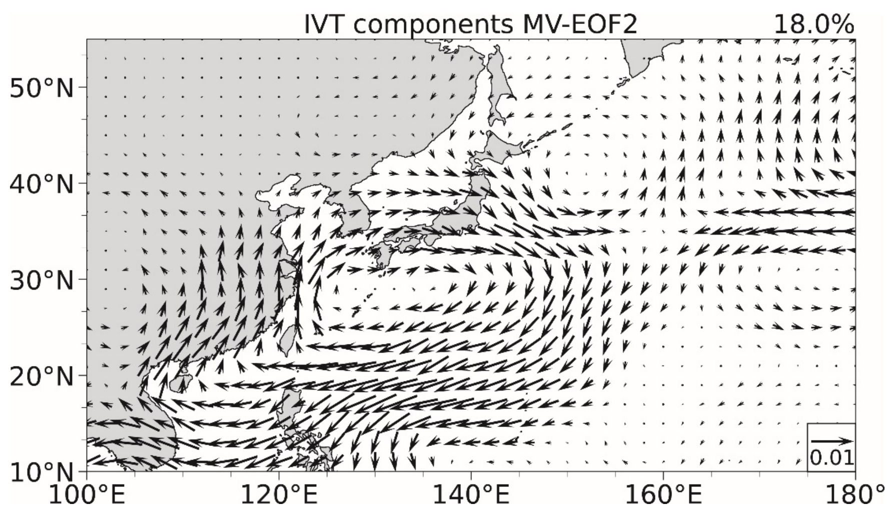

Figure S4. A second MV-EOF mode sample of JJA-mean IVT over EA and WNP for the period of 1959-2021.

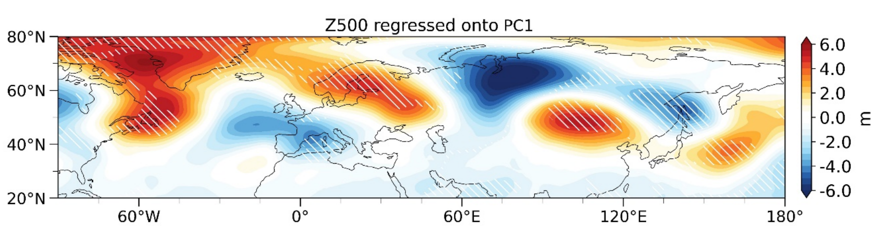

Figure S5. JJA-mean 500 hPa geopotential height regressed onto PC1. White hatches denote the area with a 95% significance level.

Posted on 24 Nov 2022 — CC-BY-NC 4 — https://doi.org/10.1002/essoar.10512565.1 — This a preprint and has not been peer reviewed. Data may be preliminary.

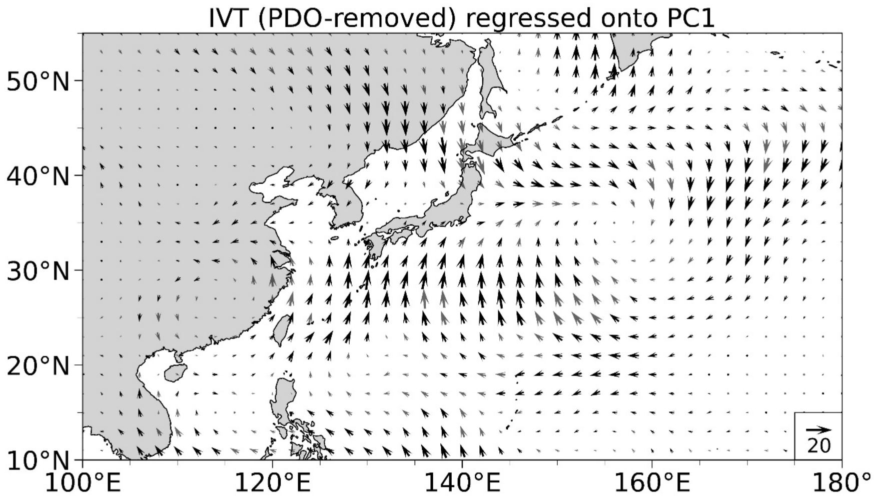

Figure S6. IVT (PDO-removed) regressed onto PC1. Black vectors denote the winds with a 95% significance level.

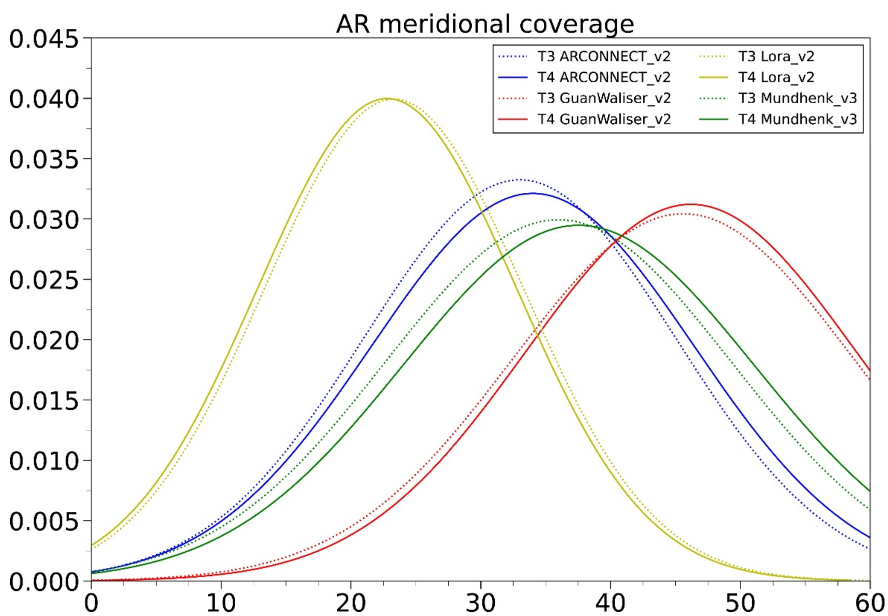

Figure S7. The probability distribution of JJA-mean AR meridional coverage (degrees) during T3 (1980-1996) and T4 (1997-2019) from four AR detection algorithms.

Table S1. Basic information of AR detection algorithms used in this study. More details are in https://www.cgd.ucar.edu/projects/artmip/algorithms.html.

Algorithm	**Threshold**
ARCONNECT_v2	Absolute: IVT use 700 kgm-1s-1 for seeding, 300 kgm-1s-1 for region growing
Guan_Waliser_v2	Relative: 85th percentile IVT; Absolute min requirement designed for polar locations: 100kgm-1s-1 IV'
Lora_v2	Relative/Absolute: IVT use 225 kgm-1s-1 above time/latitude dependent threshold using 30-day Runn
Mundhenk_v3	Relative IVT percentiles and/or anomalies both temporal and spatial

Posted on 24 Nov 2022 — CC-BY-NC 4 — https://doi.org/10.1002/essoar.10512565.1 — This a preprint and has not been peer reviewed. Data may be preliminary.

Algorithm	Threshold
ClimateNet	Threshold free; input fields are IWV, U850, V850, SLP

Hosted file

essoar.10512565.1.docx available at https://authorea.com/users/549897/articles/603778-opposite-interdecadal-trends-of-summer-atmospheric-rivers-over-east-asia-and-western-north-pacific-in-recent-decades

Posted on 24 Nov 2022 — CC-BY-NC 4 — https://doi.org/10.1002/essoar.10512565.1 — This a preprint and has not been peer reviewed. Data may be preliminary.

Opposite Interdecadal Trends of Summer Atmospheric Rivers over East Asia and Western North Pacific in Recent Decades

Wenshuo Huang[1], Lijuan Hua[1], Linhao Zhong[2], Yang Yang[2] and Zhaohui Gong[3,4]

[1]College of Earth and Planetary Sciences, University of Chinese Academy of Sciences, Beijing 100049, China

[2]National Institute of Natural Hazards, Ministry of Emergency Management of China, Beijing 100085, China

[3]University of Chinese Academy of Sciences, Beijing 100049, China

[4]CAS Key Laboratory of Regional Climate-Environment for Temperate East Asia, Institute of Atmospheric Physics, Chinese Academy of Sciences, Beijing 100029, China

Corresponding author: Wenshuo Huang (huangwenshuo21@mails.ucas.edu.cn)

Key Points:

- Summer atmospheric rivers (ARs) over East Asia and Western North Pacific experienced opposite interdecadal trends in recent four decades.
- The opposite AR variations significantly correlate with the Pacific Decadal Oscillation and a wave train from the North Atlantic.
- AR detection algorithms trained with historical AR shapes should be used cautiously for the AR geometric features may differ from the past.

Abstract

The summer atmospheric river (AR) frequency over East Asia and Western North Pacific (EA-WNP) is investigated by multiple AR detection algorithms based on the Atmospheric River Tracking Method Intercomparison Project (ARTMIP) Tier2 reanalysis dataset. The results show that AR frequency during the recent four decades experienced opposite interdecadal shifts, greatly contributing to the interdecadal equatorward trends of EA ARs and poleward trends of WNP ARs with a boundary around 135°E. The opposite variations are mainly influenced by a zonal dipole of integrated water vapor transport with cyclonic and anticyclonic anomalies centered over Taiwan and the ocean to the southeast of Japan, respectively. A major impact of the Pacific Decadal Oscillation and a reinforcement effect due to a zonal wave train from the North Atlantic jointly modulate the pattern. Considering ARs may curve their pathway over EA-WNP, the algorithms based on historical AR shapes should be cautiously used during AR detection.

Plain Language Summary

The atmospheric rivers (ARs) are long, narrow corridors of intense water vapor transport related to extreme precipitation events and floods. Previous research showed the long-term southward trends of ARs over East Asia (EA). However, in this study, since EA ARs usually extend westward to more than 180°E over East Asia and Western North Pacific (EA-WNP), we examined summer EA-WNP ARs and found that they actually experienced opposite interdecadal trends in the past four decades through multiple AR detection algorithms, which were the results of opposite interdecadal AR variations. The interdecadal shifts are explained by a zonal dipole pattern of integrated water vapor transport circulation, which is modulated by a major influence of the Pacific Decadal Oscillation and an intensification influence of atmospheric teleconnection wave train from the North Atlantic. The analysis results also suggest that ARs may curve their pathway over EA-WNP, and the AR detection algorithms with a criterion of historical AR shapes should be used with caution during AR detection in the future.

1 Introduction

Atmospheric rivers (ARs) are filamentary-shaped corridors of intensive water vapor transport responsible for conveying nearly 90% of the water vapor from the tropics to the poles (Newell et al., 1992; Zhu & Newell, 1994, 1998). Since the 21st century, a large number of extreme rainfall events and floods over midlatitudes have been linked to the irreplaceable contribution of ARs (Collow et al., 2020; Dettinger et al., 2011; Leung & Qian, 2009; Ralph et al., 2006, 2019). ARs could also affect the variations of Arctic and Antarctic sea ice by transporting warm moisture from lower latitudes (Baggett et al., 2016; Hegyi & Taylor, 2018; Li et al., 2022; Wille et al., 2022). Therefore, it is necessary to improve the understanding of AR characteristics, particularly the changes of AR distribution which could significantly influence the hydrological cycle and water balance between different latitudes.

Considerable efforts have been made to study the changes of AR distribution in North America and Europe. Payne and Magnusdottir (2015) found equatorward trends of ARs under a warming world on the west coasts of North America. European ARs were suggested to move southward in future projections (Gao et al., 2016). Shields and Kiehl (2016) showed that landfalling ARs are expected to shift southward in winter and northward in summer. In the Southern Hemisphere, the observation and simulation of ARs are increasing at higher-latitude regions primarily due to a poleward shift of westerly jet (Ma et al., 2020). But in recent years, there is also growing scientific concentration on East Asia (EA) ARs. ARs are associated with EA summer monsoon and have the potential predictability of extreme precipitation over EA (Pan & Lu, 2020; Park et al., 2021; Wang et al., 2021). Concerning the AR trends in EA, Liang et al. (2022) pointed out that the southward shift of historical ARs is related to the alteration of boreal summer southwesterly monsoon flow. However, AR is generally more than 2000 kilometers long and could be influenced by various systems, while EA ARs could always extend to Western North Pacific (WNP) region (Pan & Lu, 2020). Hence, whether the ARs have consistent trends over the holistic EA and Western North Pacific (referred to as EA-WNP hereafter) region remain understudied.

Meanwhile, previous studies have shown that internal climate variability could influence ARs over EA. Liang and Yong (2021) presented the interannual variability of ARs associated with the combination of the Quasi-Biennial Oscillation and the El Niño–Southern Oscillation, Kamae et al. (2017) noted that the northward shift of ARs in the boreal summer was preceded by a winter El Niño event. Yet the impact of interdecadal variability on ARs over EA is still not clear, since many studies (Huang et al., 2019; Si & Ding, 2016; Zhang et al., 2018) indicated that interdecadal variability such as Pacific Decadal Oscillation (PDO) and Atlantic Multidecadal Oscillation (AMO) could cause significant shifts to the EA summer monsoon and precipitation, In this respect, we aim to explore the relationship between EA-WNP ARs and interdecadal variability.

In our study, we examined the holistic EA-WNP summer AR frequency. Interestingly, opposite interdecadal trends and shifts were found that differed from the unidirectional trends over EA. As such, the following analysis is organized into three parts. First, we present the specific characteristics of observed AR frequency variations over EA-WNP. Second, interdecadal variability associated with the phenomenon featuring opposite displacement is investigated. Third, some possible influence behind the AR trends and shifts is discussed. Notably, AR characteristics may vary significantly depending on the detection algorithms (O'Brien et al., 2021; Shields et al., 2018; Zhou et al., 2021). During AR trends analysis, we used the average of multiple AR detection algorithms from the Atmospheric River Tracking Method Intercomparison Project (ARTMIP) to reduce the uncertainty due to different identification methods. ARTMIP is an international collaborative project aiming to quantify and understand the uncertainties in AR detection algorithms (Shields et al., 2018).

2 Data and Methods

2.1 AR and Reanalysis Datasets

The AR detection products are from the ARTMIP Tier 2 Reanalysis catalogue (Collow et al., 2022). Considering the integrity of datasets and algorithms, we mainly use the detection derived from Version 2 of Modern-Era Retrospective analysis for Research and Applications (MERRA-2) at 0.5° × 0.625° (Gelaro et al., 2017). And 1-hourly MERRA-2 is resampled to 6-hourly to reduce computation which has little effect on the climatology. The analyzed AR trends are further supplementally verified by another dataset JRA-55 at 1.25° × 1.25° from the Japan Meteorological Agency (JMA; Kobayashi et al., 2015). Four AR detection algorithms are selected and averaged to represent a relatively reliable result including ARCONNECT_v2 (Shearer et al., 2020), Guan_Waliser_v2 (Guan & Waliser, 2015; Guan et al., 2018), Lora_v2

(Lora et al., 2017; Skinner et al., 2020) and Mundhenk_v3 (Mundhenk et al., 2016). These algorithms are all designed for global regions without a specific area mask and take different types of integrated water vapor transport (IVT) thresholds during AR detection (referring to Table S1 for detailed information). IVT is generally used as the metric for measuring ARs and is calculated as the vector magnitude of $\overrightarrow{\mathrm{IVT}}$, $\overrightarrow{\mathrm{IVT}}$ is defined as:

$$\overrightarrow{\mathrm{IVT}} = -\frac{1}{g}\left\langle \int_{p_0}^{p_{\mathrm{top}}} qudp, \int_{p_0}^{p_{\mathrm{top}}} qvdp \right\rangle \#(1)$$

where g is the acceleration of gravity, u and v are horizontal wind components, q is specific humidity. Empirically, p_0 is 1000 hPa and p_{top} is 200 hPa or 300 hPa with enough pressure levels containing most of the moisture to detect ARs. Besides, another AR algorithm ClimateNet (Prabhat et al., 2020) (See Table S1) based on deep learning and trained by expert-labeled AR images is also compared at the end of the article.

For analyzing associated atmospheric circulation environments, the latest ERA5 reanalysis data at 0.25° × 0.25° from the European Centre for Medium-range Weather Forecasts (ECMWF; Hersbach et al., 2020) is used, which covers the periods from 1959 to the present. ERA5 products from 1959 onwards are not suffered from the unrealistically intense tropical cyclones in contrast to the preliminary version of ERA5 back extension 1950-1978 (Bell et al., 2021). The variables include the IVT components to extract the dominant mode from AR trends, horizontal wind components, vertical velocity, and geopotential height for examining the circulation configuration. The vorticity was calculated through spherical harmonics with T42 truncations from zonal and meridional components as in (Wu et al., 2016) to present a clear spatial pattern. While the SST dataset was obtained from the National Oceanic and Atmospheric Administration (NOAA) Extended Reconstructed Sea Surface Temperature version 5 (ERSSTv5; Huang et al., 2017). And the PDO index was provided by the National Centers for Environmental Information (NCEI). The range of study period for the large-circulation environments from ERA5 is 1959-2021 to get enough length for deriving long-term interdecadal variability. When further analyzing the mechanism behind observed interdecadal AR trends and shifts over EA-WNP, only 1980-2019 is considered due to the limitation of AR detection data length. Concerning ARs mostly happen in summer over EA (Liang & Yong, 2021; Pan & Lu, 2020), we focus on the June-August (JJA) mean.

2.2 Methodology

Given the 6-hourly AR dataset, we calculate the proportion of time for a grid cell experiencing AR events during summer as AR frequency. Then 0.25 times the frequency is regarded as an equivalent AR day because of the 6-hourly AR detection data following (O'Brien et al., 2021). All the datasets were performing a 7-year moving average first as in (Xie & Wang, 2020) to concentrate on the interdecadal variability, and then the trend associated with global warming in atmospheric circulation environments was removed using the global-mean SST following (Mann & Emanuel, 2006; Ting et al., 2009). In order to extract the dominant signal of the AR trends, multivariate empirical orthogonal function (MV-EOF) analysis was introduced to IVT components, which could extract correlated spatial patterns from multi-field data (Wang, 1992). The atmospheric circulation environments and SST anomalies patterns associated with the dominant signal of AR trend were derived by regressing filtered interdecadal fields onto the normalized time series of the dominant principal component. In addition, the horizontal wave activity flux (WAF) was used to diagnose the energy propagation directions of stationary Rossby waves following (Wu et al., 2016; Z. Zhang et al., 2018). Specific details are available in (Takaya & Nakamura, 2001).

The significance test in this study contained a two-tailed Student's t-test for regression and correlation coefficient and a modified Mann-Kendall test (Yue & Wang, 2004) for trend analysis. Since time series may have high autocorrelations after low-pass filtering, the number of degrees of freedom is decreased and the number of effective degrees of freedom from (Chen, 1982; Davis, 1976) is used during the significance test.

3 Results

3.1 **Characteristics of Opposite Interdecadal ARs Trends and Shifts in East Asia and Western North Pacific**

The climatology and variations of AR frequency over EA-WNP detected from MERRA-2 are shown in Figure 1. Figure 1a provides the climatological (1980-2019) AR frequency in summer over EA-WNP. The majority of ARs occur in the midlatitudes between 20°N and 50°N along a southwest-northeast strip extending to 180°E in summer, suggesting that both EA and WNP regions should be considered when analyzing AR features. Figure 1b displays the interdecadal trends of the observed AR frequency in the past four decades. The most salient feature is that ARs present opposite tendencies between EA and WNP with a boundary around 135°E, i.e., a southward displacement over EA but northward over WNP. Therefore, we defined ARs west of 135°E as EA ARs and east of 135°E as WNP ARs. EA ARs show the same equatorward trend as the conclusion from (Liang et al., 2022), but WNP AR trend is poleward to the contrary. The opposite trends are also detected through verification from JRA-55 (Figure S1). Meanwhile, though different AR detection algorithms can influence the AR frequency, four methods in analysis all show similar trends pattern (Figures S2), which indicates that the ARs over EA-WNP do experience opposite trends in the past 40 years.

Therefore, we select four 5° × 5° boxes: E1 (30°–35°N, 115°–120°E), E2 (20°–25°N, 120°–125°E), W1 (40°–45°N, 155°–160°E), and W2 (35°–40°N, 170°–175°E) to approximately represent the interdecadal variations of EA and WNP ARs (shown in Figure 1b). The corresponding AR index is defined as the normalized area-weighted mean of interdecadal AR frequency in each box (Figures 1c and 1d). Despite the opposite shift directions, the phase transitions of the EA ARs (E1 and E2) and WNP ARs (W1 and W2) time series consistently took place around the mid-to-late 1990s. Four indexes all pass the modified Mann-Kendall test (Figures 1c and 1d), which also show the interdecadal shifts resulting in the opposite interdecadal trends in Figure 1b. The time of phase transition suggests the possible connection with PDO, whose phase transition also occurred in the mid-to-late 1990s and has been proved to be crucial to the climate in East Asia (Mantua & Hare, 2002; Zhu et al., 2011; Z. Zhang et al., 2018; G. Zhang et al., 2020). The observed AR variations are actually the joint contributions of internal variability and external forcing such as global warming. However, due to the opposite shifts remarkably synchronized with PDO variation, we next mainly investigate the impacts of interdecadal climate variability on the opposite shifts. And how ARs over EA and WNP respond to climate change are worth future exploring.

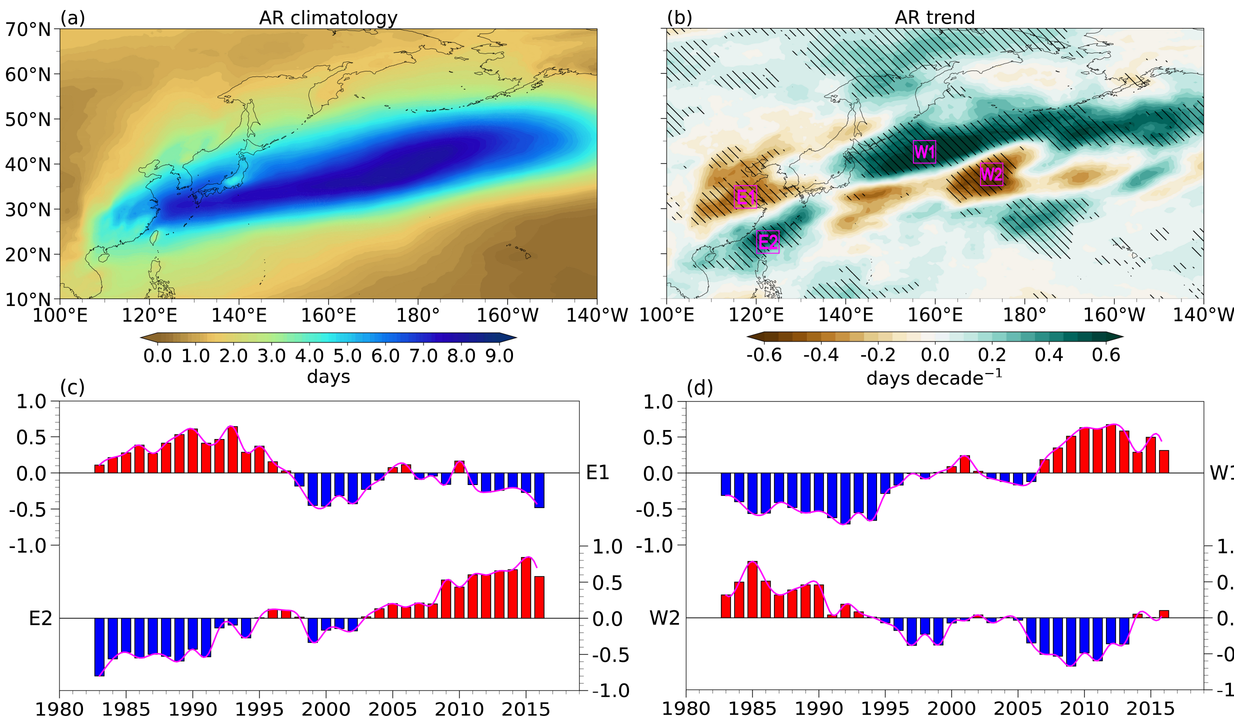

Figure 1. (a) Spatial distribution of climatological AR frequency during the summer of 1980-2019. (b) Linear trends of JJA-mean AR frequency based on multiple AR detection algorithms average. Red boxes define the index in (c) and (d): E1 (30°–35°N, 115°–120°E), E2 (20°–25°N, 120°–125°E), W1 (40°–45°N, 155°–160°E), and W2 (35°–40°N, 170°–175°E). (c) Normalized time series of JJA-mean EA AR index (E1 and E2). (d) As in (c) but for WNP ARs (W1 and W2). Black hatches in (b) denote the area with a 95% significance level.

3.2 Impacts of Interdecadal Variability on the Opposite Interdecadal AR shifts

To identify the possible reason behind the opposite interdecadal AR shifts, MV-EOF was applied to the detrended interdecadal IVT components over EA-WNP region (10°–55°N, 100°–180°E) during 1959-2021. The leading MV-EOF mode is shown in Figure 2a which accounts for 22.3% of the total variance. For the spatial configuration, there is an anomalous cyclonic IVT circulation centered nearby Taiwan and a larger anomalous anticyclonic IVT circulation centered nearby the ocean to the southeast of Japan. Interestingly, this asymmetric dipole of IVT circulation structure also takes around 135°E as the border resembles the AR trends in Figure 1b. The sensitivity of the MV-EOF decomposition to the choice of analysis domain is also examined with three different domains: a northern domain (20°–70°N, 100°–180°E), an eastern domain (10°–60°N, 110°E–160°W), and a western domain (10°–60°N, 80°–180°E) (Figure S3). The resultant three leading modes all reproduce the same dipole IVT configuration as that for the origin domain though some differences exist in the second MV-EOF modes (Figure S4), which manifests the robusticity of the mode shown in Figure 2a. Figure 2b exhibits the normalized time series of the leading principal component (PC1) and the normalized JJA-mean PDO index. Generally, PC1 fluctuates in the inverse phase of the PDO with a significant correlation of −0.733 at the 95% confidence level. During the past four decades, PC1 and PDO changed from a negative-phase PC1 ($PC1^{-}$) and a positive-phase PDO (PDO^{+}) to a positive-phase PC1 ($PC1^{+}$) and a negative-phase PDO (PDO^{-}), which modulated the anticyclonic IVT anomalies transfer to cyclonic IVT anomalies over EA and cyclonic IVT anomalies transfer to anticyclonic IVT anomalies over WNP. Furthermore, the JJA-mean global SST was regressed onto PC1 (Figure 2c), and the SST anomalies in the Pacific present a PDO-like pattern (in cold phase) with warm SST anomalies in the midlatitude North Pacific and cold anomalies in the tropical Pacific and on the west coast of North America. These results reveal that the leading IVT pattern is tightly associated with the interdecadal variability of PDO. Meanwhile, there also exist SST signals in the North Atlantic (NA), particularly those near the Labrador Sea.

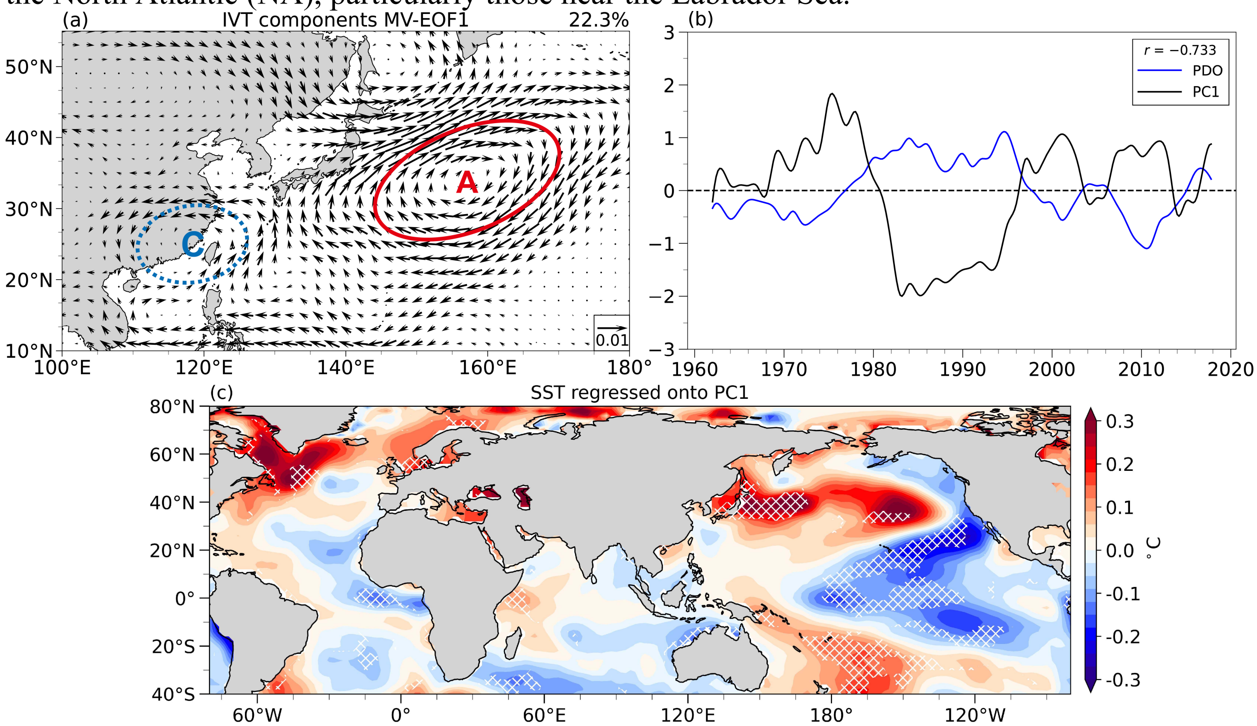

Figure 2. (a) The leading MV-EOF mode of JJA-mean IVT over EA-WNP region (10°–55°N, 100°–180°E) for the period of 1959-2021 in which variability less than 7-year and global-mean SST trend have been removed (kg m-1s-1). The fractional variance explained is marked at the top-right corner. (b) Normalized time series of PC1 (black line) and JJA-mean PDO index (blue line). (c) The JJA-mean SST regressed onto PC1 (°C). White hatches in (c) denote the area with a 95% significance level.

Figure 3a demonstrates the impact of PC1 on observed ARs. The related AR frequency shows a high similarity with the opposite variations in Figure 1b. In reality, IVT essentially determined ARs during detection so that the opposite interdecadal AR trends and shifts over EA-WNP could be well explained, as the direction of ARs flow in the midlatitudes of the northern hemisphere is generally eastward due to the westerlies, the eastward IVT anomalies could enhance the occurrence of ARs while the westward IVT anomalies play an adverse role. For the interdecadal shift in EA ARs, during $PC1^{-}$ period (anticyclonic IVT), there were abnormal more ARs in E1 (westward IVT anomalies) and abnormal less ARs in E2 (eastward IVT anomalies). During the cyclonic IVT period ($PC1^{+}$), there were abnormal less ARs in E1 (eastward IVT anomalies) and abnormal more ARs in E2 (westward IVT anomalies). The interdecadal shifts of WNP ARs are induced by the same response mechanism. Simply put, the interdecadal change of zonal components in anomalous cyclone (anticyclone) contributes substantially to the observed opposite interdecadal AR shifts.

Further investigation in Figure 3b proves that the PDO^{-} drives a highly consistent dipole pattern as MV-EOF1 mode (Figure 2a), corresponding to the positive vorticity anomalies centered over Taiwan and negative vorticity anomalies centered over the ocean to the southeast of Japan at 850 hPa. As noted in many previous studies, the ocean to the southeast of Japan is characterized by an anomalous cyclone during PDO^{+} and an anomalous anticyclone during PDO^{-} at the low-level atmospheric circulation, which may as a consequence of the upstream wave trains and the midlatitude air-sea interactions from local SST anomalies (Frankignoul & Sennéchael, 2007; Fang & Yang, 2016; Zhu et al., 2008; Zhang et al., 2018). At the same time, the vorticity anomalies along the coast of East China in Figure 3b bear some resemblance to the interdecadal Pacific-Japan (PJ) pattern, which does not show the eastward feature compared to the convectional PJ pattern (Nitta, 1987; Wu et al., 2016; Xie et al., 2022). Together with horizontal anomalies, the associated atmospheric meridional circulation calculated by zonal (115°–130°E) averaged (Figure 3c) also exhibits similar anomalous convective heating from the maritime continent, which is reckoned to be responsible for the origin of the interdecadal PJ pattern (Xie et al., 2022).

In addition, as for the SST anomalies in NA found in Figure 2c, Figure 3d presents the geopotential heights at 300 hPa related to the PC1 (the results at 500 hPa are similar in Figure S5) and corresponding horizontal WAF. From the viewpoint of atmospheric teleconnection, there is a wave train from NA to WNP with significant positive (negative) anomalies of Z300 over the WNP during $PC1^{+}$ ($PC1^{-}$). Removing the PDO-related signal in IVT, the PC1-related circulation shows weaker anticyclonic IVT anomalies compared to Figure 3b (Figure S6), which shows the teleconnection could reinforce the circulation anomalies over the ocean to the southeast of Japan on the interdecadal time scale.

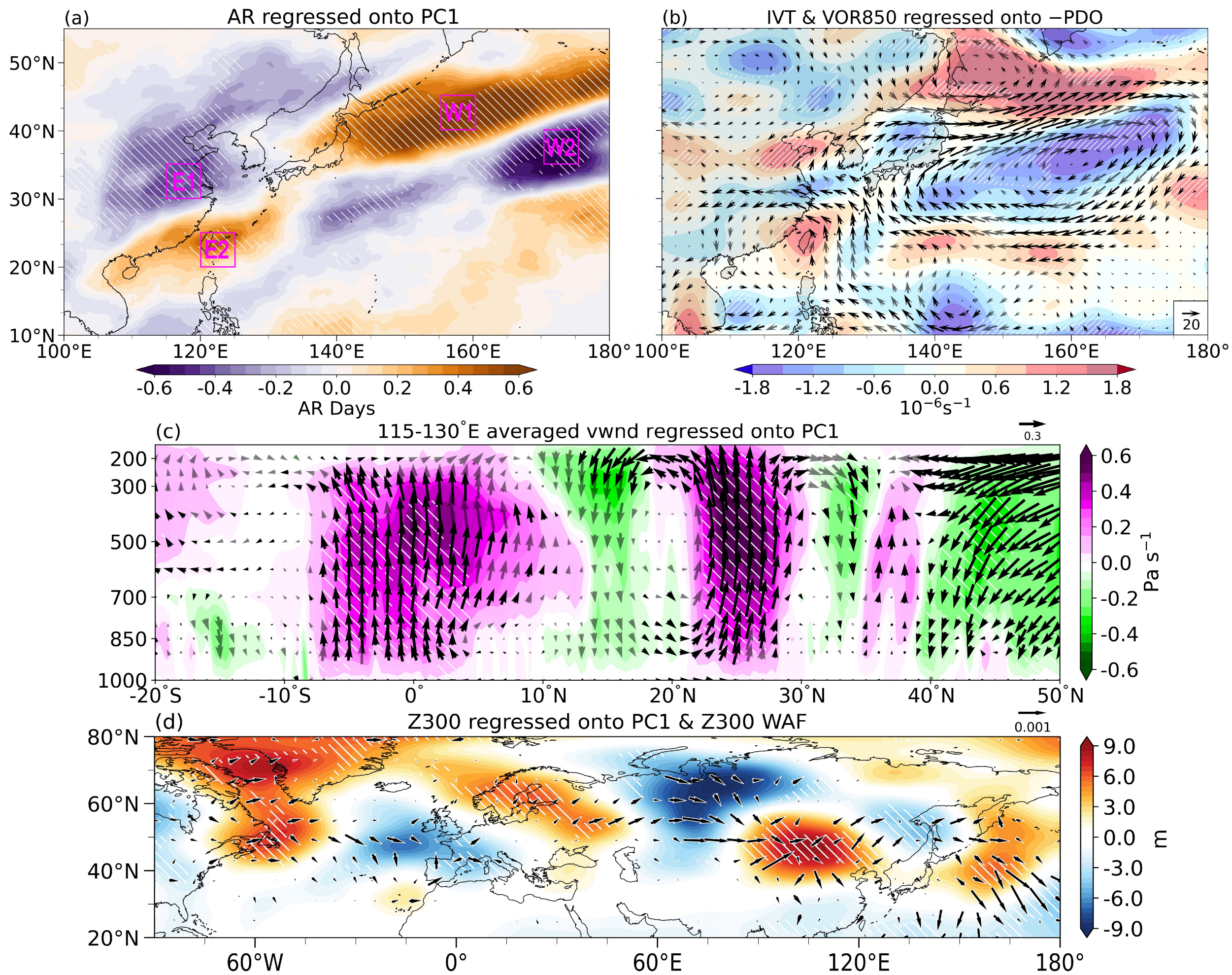

Figure 3. (a) JJA-mean AR frequency regressed onto PC1 during 1980-2019. (b) JJA-mean IVT components (vectors, kg m-1s-1) and 850 hPa vorticity (shading) regressed onto PDO− index. (c) JJA-mean atmospheric meridional circulation calculated from the meridional wind (horizontal component of vectors, m s-1) and vertical velocity (vertical component of vectors and shading, Pa s-1) regressed onto PC1. The vertical velocity is amplified 100 times in plot. (d) JJA-mean 300 hPa geopotential height regressed onto PC1 (shading) with corresponding wave activity flux (vectors, m-2 s-2). Black vectors in (b) and (c) denote the winds with a 95% significance level. White hatches in (a)-(d) denote the area with a 95% significance level.

3.3 Possible Influence of the Opposite Trends and Shifts

Given the opposite trends discussed above, the strengthened cyclonic anomalies over Taiwan and anticyclonic anomalies over the ocean to the southeast of Japan are crucial to push the AR moving southward over EA but poleward over WNP in the past four decades, as shown by the green pathway in Figure 4a. Statistically, AR generally appears in the form of a continuous band of strong moisture transport extending from EA to WNP, which implies the opposite displacements of AR trends may result from the regional meander of AR pathway. The opposite trends and shifts bring about a longer meridional pathways of ARs compared to the initial state. Accordingly, we calculate the meridional coverage of AR at each snapshot through

6-hourly AR detection data from each algorithm. The AR meridional coverage here is defined as the latitude difference between the northernmost and southernmost grid of AR at each snapshot. Figure 4b compares the probability distribution of the AR meridional distance in the first and last decade. Most algorithms display an increasing meridional distance except that Lora_v2 does not change significantly. The meridional variation analyzed from ARCONNECT_v2 even reaches about 5 degrees. And the probability distribution before and after the mid-late 1990s in Figure S7 also provides a similar tendency.

The curvature of AR pathway could also affect the accuracy of AR detection algorithms based on AR shapes. As a demonstration, we also analyzed the JJA-mean AR trends during the same period from a deep learning algorithm ClimateNet, which mainly used the relatively straight geometric shapes of historical IVT as the training dataset. Figure 4c shows that the analysis from ClimateNet could only present a poleward shifting as the main body of the ARs in contrast to Figure 1b. These results indicate that future AR detection should pay more attention to those algorithms based on AR geometric shapes over EA-WNP.

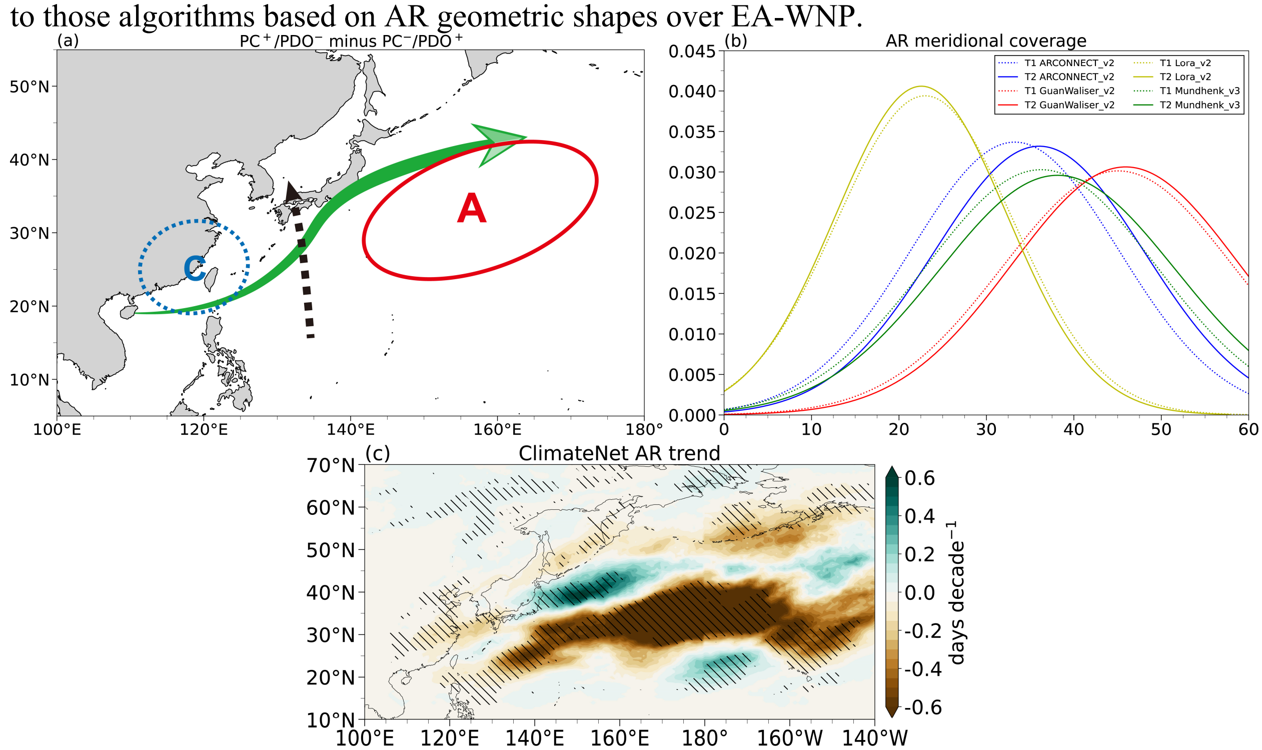

Figure 4. (a) Schematic diagram for the opposite trends and shifts of JJA-mean ARs. While the dashed blue (solid red) circle indicates the cyclonic (anticyclonic) IVT circulation anomalies. The green solid arrow denotes the AR flow and the black dashed arrow denotes the northward IVT anomalies near 135°E. (b) The probability distribution of JJA-mean AR meridional coverage (degrees) during T1 (1980-1989) and T2 (2010-2019) from four AR detection algorithms. (c) JJA-mean AR trends analyzed from ClimateNet. Black hatches in (c) denote the area with a 95% significance level.

4 Conclusions

Based on the ARTMIP Tier 2 reanalysis dataset, we investigated the summertime ARs over EA-WNP in the past four decades. Opposite interdecadal trends as equatorward EA ARs and poleward WNP ARs with the same interdecadal variations that occurred in the mid-late 1990s are found. To analyze the dominant signal behind the opposite interdecadal variations, MV-EOF is applied to IVT components and reveals a zonal dipole pattern which also takes 135°E as a boundary compared to the observed variations. Analysis shows that interdecadal IVT circulation transition for cyclonic to anticyclonic anomalies over Taiwan and anticyclonic to cyclonic anomalies over ocean to the southeast of Japan are responsible for the opposite interdecadal AR shifts. Because of the original eastward direction of ARs flow over EA-WNP, the eastward and westward IVT anomalies of the cyclonic (anticyclonic) circulation components could induce interdecadal shifts, which result in AR meridional displacement. Further study present that the dipole structure is modulated by a major influence of the PDO and an intensification influence of atmospheric teleconnection wave train from the North Atlantic in the interdecadal time scale.

Other features such as the geometric shapes and meridional coverage of ARs may be changing over the recent decades under the opposite trends and shifts. Large sample statistical analysis during the decades present AR meridional coverage is increasing. Considering the effect of the above evidence, we compare the interdecadal trends derived from ClimateNet based on AR geometric shapes, showing that those AR detection algorithms with a criterion of AR shapes may not be able to capture the opposite characteristics and should be implemented cautiously over EA-WNP in the future AR detection. Future research might explore how the AR frequency variations over EA-WNP are affected by external forcings and quantify the relative contribution between different factors. Investigations also should be undertaken for whether the opposite trends could occur in other areas.

Acknowledgments

We acknowledge the community effort from ARTMIP. Co-chairs and committee members include Jonathan Rutz, Christine Shields, L. Ruby Leung, F. Martin Ralph, Michael Wehner, Ashley Payne, Travis O'Brien, and Allison Collow. ARTMIP has received support from the US Department of Energy Office of Science Biological and Environmental Research (BER) as part of the Regional and Global Climate Modeling program, and the Center for Western Weather and Water Extremes (CW3E) at Scripps Institute for Oceanography at the University of California, San Diego. This work was supported by the National Natural Science Foundation of China (NSFC) under Grants No. 42275183, 42275043, and 42130613.

Open Research

The ARTMIP Tier 2 catalogues for Reanalysis Intercomparison are available from the Climate Data Gateway DOI: https://10.0.101.168/rawv-yx53. ERA5 data could be downloaded from the Copernicus Climate Change Service (C3S) Climate Data Store at https://cds.climate.copernicus.eu/. SST dataset ERSSTv5 was provided by the NOAA PSL from https://psl.noaa.gov/data/gridded/data.noaa.ersst.v5.html. The PDO index could be found from the NOAA NCEI at https://www.ncei.noaa.gov/access/monitoring/pdo/.

References

Baggett, C., Lee, S., & Feldstein, S. (2016). An Investigation of the Presence of Atmospheric Rivers over the North Pacific during Planetary-Scale Wave Life Cycles and Their Role in

Arctic Warming. *Journal of the Atmospheric Sciences*, *73*(11), 4329–4347. https://doi.org/10.1175/JAS-D-16-0033.1

Bell, B., Hersbach, H., Simmons, A., Berrisford, P., Dahlgren, P., Horányi, A., Muñoz-Sabater, J., Nicolas, J., Radu, R., Schepers, D., Soci, C., Villaume, S., Bidlot, J.-R., Haimberger, L., Woollen, J., Buontempo, C., & Thépaut, J.-N. (2021). The ERA5 global reanalysis: Preliminary extension to 1950. *Quarterly Journal of the Royal Meteorological Society*, *147*(741), 4186–4227. https://doi.org/10.1002/qj.4174

Chen, W. Y. (1982). Fluctuations in Northern Hemisphere 700 mb Height Field Associated with the Southern Oscillation. *Monthly Weather Review*, *110*(7), 808–823. https://doi.org/10.1175/1520-0493(1982)110<0808:FINHMH>2.0.CO;2

Collow, A. B. M., Mersiovsky, H., & Bosilovich, M. G. (2020). Large-Scale Influences on Atmospheric River–Induced Extreme Precipitation Events along the Coast of Washington State. *Journal of Hydrometeorology*, *21*(9), 2139–2156. https://doi.org/10.1175/JHM-D-19-0272.1

Collow, A. B. M., Shields, C. A., Guan, B., Kim, S., Lora, J. M., McClenny, E. E., Nardi, K., Payne, A., Reid, K., Shearer, E. J., Tomé, R., Wille, J. D., Ramos, A. M., Gorodetskaya, I. V., Leung, L. R., O'Brien, T. A., Ralph, F. M., Rutz, J., Ullrich, P. A., & Wehner, M. (2022). An Overview of ARTMIP's Tier 2 Reanalysis Intercomparison: Uncertainty in the Detection of Atmospheric Rivers and Their Associated Precipitation. *Journal of Geophysical Research: Atmospheres*, *127*(8). https://doi.org/10.1029/2021JD036155

Davis, R. E. (1976). Predictability of Sea Surface Temperature and Sea Level Pressure Anomalies over the North Pacific Ocean. *Journal of Physical Oceanography*, *6*(3), 249–266. https://doi.org/10.1175/1520-0485(1976)006<0249:POSSTA>2.0.CO;2

Dettinger, M. D., Ralph, F. M., Das, T., Neiman, P. J., & Cayan, D. R. (2011). Atmospheric Rivers, Floods and the Water Resources of California. *Water*, *3*(2), 445–478. https://doi.org/10.3390/w3020445

Fang, J., & Yang, X.-Q. (2016). Structure and dynamics of decadal anomalies in the wintertime midlatitude North Pacific ocean–atmosphere system. *Climate Dynamics*, *47*(5), 1989–2007. https://doi.org/10.1007/s00382-015-2946-x

Frankignoul, C., & Sennéchael, N. (2007). Observed Influence of North Pacific SST Anomalies on the Atmospheric Circulation. *Journal of Climate*, *20*(3), 592–606. https://doi.org/10.1175/JCLI4021.1

Gao, Y., Lu, J., & Leung, L. R. (2016). Uncertainties in Projecting Future Changes in Atmospheric Rivers and Their Impacts on Heavy Precipitation over Europe. *Journal of Climate*, *29*(18), 6711–6726. https://doi.org/10.1175/JCLI-D-16-0088.1

Gelaro, R., McCarty, W., Suárez, M. J., Todling, R., Molod, A., Takacs, L., Randles, C. A., Darmenov, A., Bosilovich, M. G., Reichle, R., Wargan, K., Coy, L., Cullather, R., Draper, C., Akella, S., Buchard, V., Conaty, A., Silva, A. M. da, Gu, W., … Zhao, B. (2017). The Modern-Era Retrospective Analysis for Research and Applications, Version 2 (MERRA-2). *Journal of Climate*, *30*(14), 5419–5454. https://doi.org/10.1175/JCLI-D-16-0758.1

Guan, B., & Waliser, D. E. (2015). Detection of atmospheric rivers: Evaluation and application of an algorithm for global studies: Detection of Atmospheric Rivers. *Journal of Geophysical Research: Atmospheres*, *120*(24), 12514–12535. https://doi.org/10.1002/2015JD024257

Guan, B., Waliser, D. E., & Ralph, F. M. (2018). An Intercomparison between Reanalysis and Dropsonde Observations of the Total Water Vapor Transport in Individual Atmospheric Rivers. *Journal of Hydrometeorology*, *19*(2), 321–337. https://doi.org/10.1175/JHM-D-17-0114.1

Hegyi, B. M., & Taylor, P. C. (2018). The Unprecedented 2016–2017 Arctic Sea Ice Growth Season: The Crucial Role of Atmospheric Rivers and Longwave Fluxes. *Geophysical Research Letters*, *45*(10), 5204–5212. https://doi.org/10.1029/2017GL076717

Hersbach, H., Bell, B., Berrisford, P., Hirahara, S., Horányi, A., Muñoz-Sabater, J., Nicolas, J., Peubey, C., Radu, R., Schepers, D., Simmons, A., Soci, C., Abdalla, S., Abellan, X., Balsamo, G., Bechtold, P., Biavati, G., Bidlot, J., Bonavita, M., … Thépaut, J.-N. (2020). The ERA5 global reanalysis. *Quarterly Journal of the Royal Meteorological Society*, *146*(730), 1999–2049. https://doi.org/10.1002/qj.3803

Huang, B., Thorne, P. W., Banzon, V. F., Boyer, T., Chepurin, G., Lawrimore, J. H., Menne, M. J., Smith, T. M., Vose, R. S., & Zhang, H.-M. (2017). Extended Reconstructed Sea Surface Temperature, Version 5 (ERSSTv5): Upgrades, Validations, and Intercomparisons. *Journal of Climate*, *30*(20), 8179–8205. https://doi.org/10.1175/JCLI-D-16-0836.1

Huang, D., Dai, A., Yang, B., Yan, P., Zhu, J., & Zhang, Y. (2019). Contributions of Different Combinations of the IPO and AMO to Recent Changes in Winter East Asian Jets. *Journal of Climate*, *32*(5), 1607–1626. https://doi.org/10.1175/JCLI-D-18-0218.1

Kamae, Y., Mei, W., Xie, S.-P., Naoi, M., & Ueda, H. (2017). Atmospheric Rivers over the Northwestern Pacific: Climatology and Interannual Variability. *Journal of Climate*, *30*(15), 5605–5619. https://doi.org/10.1175/JCLI-D-16-0875.1

Kobayashi, S., Ota, Y., Harada, Y., Ebita, A., Moriya, M., Onoda, H., Onogi, K., Kamahori, H., Kobayashi, C., Endo, H., Miyaoka, K., & Takahashi, K. (2015). The JRA-55 Reanalysis: General Specifications and Basic Characteristics. *Journal of the Meteorological Society of Japan. Ser. II*, *93*(1), 5–48. https://doi.org/10.2151/jmsj.2015-001

Leung, L. R., & Qian, Y. (2009). Atmospheric rivers induced heavy precipitation and flooding in the western US simulated by the WRF regional climate model. *Geophysical Research Letters*, *36*, L03820. https://doi.org/10.1029/2008GL036445

Li, L., Cannon, F., Mazloff, M. R., Subramanian, A. C., Wilson, A. M., & Ralph, F. M. (2022). Impact of Atmospheric Rivers on Arctic Sea Ice Variations. *EGUsphere*, 1–21. https://doi.org/10.5194/egusphere-2022-36

Liang, J., & Yong, Y. (2021). Climatology of atmospheric rivers in the Asian monsoon region. *International Journal of Climatology*, *41*, E801–E818. https://doi.org/10.1002/joc.6729

Liang, J., Yong, Y., & Hawcroft, M. K. (2022). Long-term trends in atmospheric rivers over East Asia. *Climate Dynamics*. https://doi.org/10.1007/s00382-022-06339-5

Lora, J. M., Mitchell, J. L., Risi, C., & Tripati, A. E. (2017). North Pacific atmospheric rivers and their influence on western North America at the Last Glacial Maximum. *Geophysical Research Letters*, *44*(2), 1051–1059. https://doi.org/10.1002/2016GL071541

Ma, W., Chen, G., & Guan, B. (2020). Poleward Shift of Atmospheric Rivers in the Southern Hemisphere in Recent Decades. *Geophysical Research Letters*, *47*(21). https://doi.org/10.1029/2020GL089934

Mann, M. E., & Emanuel, K. A. (2006). Atlantic hurricane trends linked to climate change. *Eos, Transactions American Geophysical Union*, *87*(24), 233–241. https://doi.org/10.1029/2006EO240001

Mantua, N. J., & Hare, S. R. (2002). The Pacific Decadal Oscillation. *Journal of Oceanography*, *58*(1), 35–44. https://doi.org/10.1023/A:1015820616384

Mundhenk, B. D., Barnes, E. A., & Maloney, E. D. (2016). All-Season Climatology and Variability of Atmospheric River Frequencies over the North Pacific. *Journal of Climate*, *29*(13), 4885–4903. https://doi.org/10.1175/JCLI-D-15-0655.1

Newell, R. E., Newell, N. E., Zhu, Y., & Scott, C. (1992). Tropospheric rivers? - A pilot study. *Geophysical Research Letters*, *19*(24), 2401–2404. https://doi.org/10.1029/92GL02916

Nitta, T. (1987). Convective Activities in the Tropical Western Pacific and Their Impact on the Northern Hemisphere Summer Circulation. *Journal of the Meteorological Society of Japan. Ser. II*, *65*(3), 373–390. https://doi.org/10.2151/jmsj1965.65.3_373

O'Brien, T. A., Wehner, M. F., Payne, A. E., Shields, C. A., Rutz, J. J., Leung, L. R., Ralph, F. M., Marquardt Collow, A. B., Gorodetskaya, I., Guan, B., Lora, J. M., McClenny, E., Nardi, K. M., Ramos, A. M., Tomé, R., Sarangi, C., Shearer, E. J., Ullrich, P., Zarzycki, C. M., … Zhou, Y. (2021). *Increases in Future AR Count and Size: Overview of the ARTMIP Tier 2 CMIP5/6 Experiment* [Preprint]. Climatology (Global Change). https://doi.org/10.1002/essoar.10504170.3

Pan, M., & Lu, M. (2020). East Asia Atmospheric River catalog: Annual Cycle, Transition Mechanism, and Precipitation. *Geophysical Research Letters*, *47*(15), e2020GL089477. https://doi.org/10.1029/2020GL089477

Park, C., Son, S., & Kim, H. (2021). Distinct Features of Atmospheric Rivers in the Early Versus Late East Asian Summer Monsoon and Their Impacts on Monsoon Rainfall. *Journal of Geophysical Research: Atmospheres*, *126*(7). https://doi.org/10.1029/2020JD033537

Payne, A. E., & Magnusdottir, G. (2015). An evaluation of atmospheric rivers over the North Pacific in CMIP5 and their response to warming under RCP 8.5. *Journal of Geophysical Research: Atmospheres*, *120*(21). https://doi.org/10.1002/2015JD023586

Prabhat, Kashinath, K., Mudigonda, M., Kim, S., Kapp-Schwoerer, L., Graubner, A., Karaismailoglu, E., von Kleist, L., Kurth, T., Greiner, A., Yang, K., Lewis, C., Chen, J., Lou, A., Chandran, S., Toms, B., Chapman, W., Dagon, K., Shields, C. A., … Collins, W. (2020). *ClimateNet: An expert-labelled open dataset and Deep Learning architecture for enabling high-precision analyses of extreme weather* [Preprint]. Earth and Space Science Informatics. https://doi.org/10.5194/gmd-2020-72

Ralph, F. M., Neiman, P. J., Wick, G. A., Gutman, S. I., Dettinger, M. D., Cayan, D. R., & White, A. B. (2006). Flooding on California's Russian River: Role of atmospheric rivers. *Geophysical Research Letters*, *33*(13). https://doi.org/10.1029/2006GL026689

Ralph, F. M., Rutz, J. J., Cordeira, J. M., Dettinger, M., Anderson, M., Reynolds, D., Schick, L. J., & Smallcomb, C. (2019). A Scale to Characterize the Strength and Impacts of Atmospheric Rivers. *Bulletin of the American Meteorological Society*, *100*(2), 269–289. https://doi.org/10.1175/BAMS-D-18-0023.1

Shearer, E. J., Nguyen, P., Sellars, S. L., Analui, B., Kawzenuk, B., Hsu, K., & Sorooshian, S. (2020). Examination of Global Midlatitude Atmospheric River Lifecycles Using an Object-Oriented Methodology. *Journal of Geophysical Research: Atmospheres*, *125*(22), e2020JD033425. https://doi.org/10.1029/2020JD033425

Shields, C. A., & Kiehl, J. T. (2016). Atmospheric river landfall-latitude changes in future climate simulations. *Geophysical Research Letters*, *43*(16), 8775–8782. https://doi.org/10.1002/2016GL070470

Shields, C. A., Rutz, J. J., Leung, L.-Y., Ralph, F. M., Wehner, M., Kawzenuk, B., Lora, J. M., McClenny, E., Osborne, T., Payne, A. E., Ullrich, P., Gershunov, A., Goldenson, N., Guan, B., Qian, Y., Ramos, A. M., Sarangi, C., Sellars, S., Gorodetskaya, I., … Nguyen, P. (2018). Atmospheric River Tracking Method Intercomparison Project (ARTMIP): Project goals and experimental design. *Geoscientific Model Development*, *11*(6), 2455–2474. https://doi.org/10.5194/gmd-11-2455-2018

Si, D., & Ding, Y. (2016). Oceanic Forcings of the Interdecadal Variability in East Asian Summer Rainfall. *Journal of Climate*, *29*(21), 7633–7649. https://doi.org/10.1175/JCLI-D-15-0792.1

Skinner, C. B., Lora, J. M., Payne, A. E., & Poulsen, C. J. (2020). Atmospheric river changes shaped mid-latitude hydroclimate since the mid-Holocene. *Earth and Planetary Science Letters*, *541*, 116293. https://doi.org/10.1016/j.epsl.2020.116293

Takaya, K., & Nakamura, H. (2001). A Formulation of a Phase-Independent Wave-Activity Flux for Stationary and Migratory Quasigeostrophic Eddies on a Zonally Varying Basic Flow. *Journal of the Atmospheric Sciences*, *58*(6), 608–627. https://doi.org/10.1175/1520-0469(2001)058<0608:AFOAPI>2.0.CO;2

Ting, M., Kushnir, Y., Seager, R., & Li, C. (2009). Forced and Internal Twentieth-Century SST Trends in the North Atlantic. *JOURNAL OF CLIMATE*, *22*, 14. https://doi.org/10.1175/2008JCLI2561.1

Wang, B. (1992). The Vertical Structure and Development of the ENSO Anomaly Mode during 1979–1989. *Journal of the Atmospheric Sciences*, *49*(8), 698–712. https://doi.org/10.1175/1520-0469(1992)049<0698:TVSADO>2.0.CO;2

Wang, T., Wei, K., & Ma, J. (2021). Atmospheric Rivers and Mei-yu Rainfall in China: A Case Study of Summer 2020. *Advances in Atmospheric Sciences*, *38*(12), 2137–2152. https://doi.org/10.1007/s00376-021-1096-9

Wille, J. D., Favier, V., Jourdain, N. C., Kittel, C., Turton, J. V., Agosta, C., Gorodetskaya, I. V., Picard, G., Codron, F., Santos, C. L.-D., Amory, C., Fettweis, X., Blanchet, J., Jomelli, V., & Berchet, A. (2022). Intense atmospheric rivers can weaken ice shelf stability at the

Antarctic Peninsula. *Communications Earth & Environment*, *3*(1), 1–14. https://doi.org/10.1038/s43247-022-00422-9

Wu, B., Zhou, T., & Li, T. (2016). Impacts of the Pacific–Japan and Circumglobal Teleconnection Patterns on the Interdecadal Variability of the East Asian Summer Monsoon. *JOURNAL OF CLIMATE*, *29*, 19. https://doi.org/10.1175/JCLI-D-15-0105.1

Xie, M., & Wang, C. (2020). Decadal Variability of the Anticyclone in the Western North Pacific. *Journal of Climate*, *33*(20), 9031–9043. https://doi.org/10.1175/JCLI-D-20-0008.1

Xie, M., Wang, C., & Chen, S. (2022). The Role of the Maritime Continent SST Anomalies in Maintaining the Pacific–Japan Pattern on Decadal Time Scales. *JOURNAL OF CLIMATE*, *35*, 17.

Yue, S., & Wang, C. (2004). The Mann-Kendall Test Modified by Effective Sample Size to Detect Trend in Serially Correlated Hydrological Series. *Water Resources Management*, *18*(3), 201–218. https://doi.org/10.1023/B:WARM.0000043140.61082.60

Zhang, G., Zeng, G., Li, C., & Yang, X. (2020). Impact of PDO and AMO on interdecadal variability in extreme high temperatures in North China over the most recent 40-year period. *Climate Dynamics*, *54*(5–6), 3003–3020. https://doi.org/10.1007/s00382-020-05155-z

Zhang, Z., Sun, X., & Yang, X.-Q. (2018). Understanding the Interdecadal Variability of East Asian Summer Monsoon Precipitation: Joint Influence of Three Oceanic Signals. *Journal of Climate*, *31*(14), 5485–5506. https://doi.org/10.1175/JCLI-D-17-0657.1

Zhou, Y., O'Brien, T. A., Ullrich, P. A., Collins, W. D., Patricola, C. M., & Rhoades, A. M. (2021). Uncertainties in Atmospheric River Lifecycles by Detection Algorithms: Climatology and Variability. *Journal of Geophysical Research: Atmospheres*, *126*(8), e2020JD033711. https://doi.org/10/gpgsgz

Zhu, Y., & Newell, R. E. (1994). Atmospheric rivers and bombs. *Geophysical Research Letters*, *21*(18), 1999–2002. https://doi.org/10.1029/94GL01710

Zhu, Y., & Newell, R. E. (1998). A Proposed Algorithm for Moisture Fluxes from Atmospheric Rivers. *Monthly Weather Review*, *126*(3), 725–735. https://doi.org/10.1175/1520-0493(1998)126<0725:APAFMF>2.0.CO;2

Zhu, Y., Wang, H., Zhou, W., & Ma, J. (2011). Recent changes in the summer precipitation pattern in East China and the background circulation. *Climate Dynamics*, *36*(7), 1463–1473. https://doi.org/10.1007/s00382-010-0852-9

Zhu, Y., Yang, X., Xie, Q., & Yu, Y. (2008). Covarying modes of the Pacific SST and northern hemispheric midlatitude atmospheric circulation anomalies during winter. *Progress in Natural Science*, *18*(10), 1261–1270. https://doi.org/10.1016/j.pnsc.2008.05.005